J Mater Sci (2010) 45:641–651
DOI 10.1007/s10853-009-3978-6

Precipitation-hardening in cast AL–Si–Cu–Mg alloys

**F. J. Tavitas-Medrano · A. M. A. Mohamed ·
J. E. Gruzleski · F. H. Samuel · H. W. Doty**

Received: 14 June 2009 / Accepted: 12 October 2009 / Published online: 30 October 2009

Abstract Age-hardenable aluminum–silicon alloys have attracted increasing attention in recent years, particularly as a result of the demand for lighter vehicles as part of the overall goal to improve fuel efficiency and to reduce vehicle emissions. Among these aluminum cast alloys, the 319-type alloys have become the object of extensive investigation considering their practical importance to the transport industry. All the experimental variables, such as solidification condition, composition, and heat treatment, are known to have an influence on precipitation behavior; precipitation-hardening, however, is the most significant of these because of the presence of excess alloying elements from the supersaturated solid solution which form fine particles and consequently act as obstacles to dislocation movement. The precipitation-hardening behavior of a Sr-modified 319-type alloy containing 0.4% Mg was investigated for this study using transmission electron microscopy. Non-conventional aging cycles were applied so as to evaluate the degree of the improvement in strength potentially obtainable. The results show that the main strengthening phase is θ-Al_2Cu occurring in the form of plates; other phases were observed as minor constituents in this alloy, including the binary β-Mg_2Si, the ternary S-$CuAlMg_2$, and the quaternary Q-$Al_5Cu_2Mg_7Si_7$.

Introduction

Aluminum–silicon–copper 319-type cast alloys are of commercial importance because of their various applications in the automotive industry. These alloys offer a combination of a high degree of achievable strength with excellent castability, light weight and good machinability with regard to both permanent molds and sand castings. These advantages make such alloys suitable for the production of pistons, engine blocks, and cylinder heads, among a number of other parts [1, 2].

This particular alloy system, however, is seldom used in its as-cast state since it yields relatively poor mechanical properties. For this reason, a number of attempts are now being made to improve these mechanical properties including chemical treatment, reducing the porosity, solid solution hardening, and precipitation-hardening [3–8]. All the experimental variables, such as solidification condition, composition, and heat treatment are known to have an influence on precipitation behavior; precipitation-hardening, however, is the most significant of these because of the presence of excess alloying elements from the supersaturated solid solution which form fine particles and consequently act as obstacles to dislocation movement [7–10].

F. J. Tavitas-Medrano · J. E. Gruzleski
Department of Mining, Metals and Materials Engineering,
McGill University, 3610 University St., Montreal, PQ H3A 2B2,
Canada

A. M. A. Mohamed · F. H. Samuel (✉)
Département des Sciences Appliquées, Université du Québec à
Chicoutimi, Chicoutimi, PQ G7H 2B1, Canada
e-mail: fhsamuel@uqac.ca

A. M. A. Mohamed
e-mail: madel@uqac.ca

A. M. A. Mohamed
Department of Metallurgical and Materials Engineering, Faculty
of Petroleum and Mining Engineering, Suez Canal University,
Box 43721, Suez, Egypt

H. W. Doty
GM Powertrain Group, Metal Casting Technology, Inc., 127 Old
Wilton Road, Milford, NH 03055, USA

Table 1 Mean chemical composition of the 319 alloy used in this study

Element	Si	Cu	Fe	Mg	Mn	Zn	Ti	Sr
wt%	6.17	3.57	0.09	0.43	0.001	0.008	0.16	0.020

Table 2 Non-conventional heat treatment regimes employed in this study

A	2 h at 190 °C + 5 h at 180 °C
B	2 h at 190 °C + 100 h at 25 °C + 3 h at 180 °C
C	24 h at 130 °C + 2 h at 240 °C
D	1 h at 170 °C + 1 h at 190 °C + 2 h at 240 °C

Cáceres [11] reported that metastable θ'-Al_2Cu is the primary strengthening phase responsible for the precipitation-hardening response produced by these alloys. Also, it has been reported that the response of the 319 alloy to artificial aging may be improved by adding Mg; thus, the findings of Ouellet and Samuel [12] indicate that the addition of 0.45% Mg enhances the response of the alloy to this specific treatment particularly in the T6 condition, where improvements of more than 40% in strength were obtained. The alloy in question contained a substantial level of Mg in comparison with alloys which had been treated at the same temperature and for the same duration of time, i.e., at 180 °C for 8 h, and which contained noticeably low levels of Mg, that is to say, about 0.06%.

Other more complex intermetallic phases may emerge, depending on the ratio of the different elements present in the alloy; such phases may include S-Al_2CuMg, Q-$Al_5Cu_2Mg_7Si_7$, and λ-$Al_5Cu_2Mg_8Si_5$ among others [9, 13–17]. The identification of these phases, however, presents a certain amount of difficulty since most of them display the morphology of needles or very fine plates. In some cases, the precipitates are extremely difficult to identify positively using only the techniques applied for this study; and there are even times when atomic resolution equipment may be required [18–20].

An extensive amount of information is available on the heat treatment and type of precipitation observed in Al–Si–Mg alloys; [21–24] alloy 319, however, belongs to the Al–Si–Cu–Mg alloy system and its aging behavior differs since more complex interactions occur than in the alloys which belong to the Al–Si–Mg system. The challenges inherent in the 319-type alloys arise from the small size of the precipitate and the complex aging response caused by the multi-components. It is important to determine the chemical composition, crystal structure, and orientation relationship as well as precipitate morphology beforehand to understand the ensuing precipitation behavior and strengthening mechanism. For this reason, an analytical transmission electron microscope (TEM) was used to identify the structure and morphology of the various precipitates observed in alloy 319 under different aging conditions (Table 1).

Experimental procedures

The 319 as-received alloys, in the form of 12.5-kg ingots, were cut into smaller pieces, cleaned, dried, and melted in a 7-kg capacity SiC crucible, using an electrical resistance furnace. The melting temperature was maintained at 750 ± 5 °C. At this temperature, controlled amounts of Mg in the form of a pure metal were added by means of a perforated graphite bell. Strontium was added as an Al-10%Sr master alloy. Table 2 shows the mean chemical composition of the alloy used in this study, as obtained from samplings for chemical analysis taken from the corresponding melts. The chemical analysis was carried out using arc spark spectroscopy at the GM facilities in Milford, NH. The molten metal was degassed using pure, dry argon injected into the melt for ~40 min by means of a rotating graphite degassing impeller, at a rotation speed of 125 rpm, to ensure homogeneous mixing of the additives.

Tensile test bars were produced by pouring the degassed molten metal at 450 °C into a preheated permanent steel mold of the ASTM B 108 type. The average Dendrite Arm Spacing (DAS) of the sample in the testing gauge was 25 µm. The test bars were separated into ten sets, each containing five bars, as follows: one set was kept in the as-cast condition, the second set was solution heat-treated at 495 °C/8 h with a heating rate of up to 93 °C/h, then quenched in warm water at 60 °C. The subsequent eight sets were submitted to artificial aging processes as follows: four sets were aged at 170 °C for seven different aging time periods of 2, 4, 6, and 8 h while the remaining four sets were aged at 240 °C for the same seven aging time periods. The solution and aging heat treatments were carried out in a forced-air Blue M Electric Furnace equipped with a programmable temperature controller which is accurate to within ±2 °C. The aging delay was less than 10 s.

A number of non-conventional aging treatments were also carried out so as to evaluate the behavior of the 319 alloy subjected to these treatments; this approach was adopted since there is some evidence reported in the literature [25–28] that non-conventional aging practices may improve the properties of wrought aluminum alloys by up to 30% in terms of tensile strength, yield strength, and hardness. A list of the non-conventional treatments used in this study is presented in Table 2.

The as-cast and heat-treated test bars were pulled to fracture at room temperature at a strain rate of 4×10^{-4}/s using a Servohydraulic MTS Mechanical Testing machine.

A strain gauge extensometer was attached to the test bar to measure percentage elongation as the load was applied. This machine was recalibrated each time any further testing was carried out.

The microhardness of the fractured tensile bars was measured. Two coupons, each 1 cm in length, were obtained from a cross-sectional area about 1 cm from the fracture surface of each bar. These coupons were mounted in cold mounting resin, then ground and polished as is typically done for metallographic samples so as to obtain a flat mirror-like surface. Five microhardness readings were taken for each coupon using a Vickers hardness tester (Future Tech, model F11-7) equipped with a diamond indenter having a square-shaped base and an angle of 136° between facets; the load used was 100 gf. The tester was checked for calibration by taking ten hardness readings on a standard test block before proceeding to measure the treated samples. For each aging condition, the average of the values obtained for four coupons is presented here together with its respective standard deviation value.

For the TEM analysis, thin foils were cut from the tensile bars using a high-precision diamond disk cutter at low speeds. These foils were mechanically polished to a thickness of ~100 μm, followed by electrolytic jet polishing in a Struers Tenupol 3 electrolytic cell. The etchant used was a solution of 30% nitric acid and 70% methanol, while the temperature was maintained at −40 °C. Observation was carried out by means of a JEOL JEM-2100F transmission electron microscope equipped with an EDAX^{TM} chemical analysis system, and operated at 200 keV.

Results and discussion

Tensile properties and microhardness measurements

Figure 1 summarizes the variations to be observed in ultimate tensile strength, yield strength, and Vickers microhardness values as obtained for the as-cast, solution heat-treated, and artificially aged alloy. It will also be observed from the figure that the aging peak is reached after the aging treatment has been applied for 8 h at 170 °C. The properties obtained as a result of this treatment cannot be improved upon further using non-conventional aging cycles such as Treatment A. It should also be noted that Treatment B does not produce any significant changes when compared to Treatment A. Aging at 240 °C reveals that the tensile strength and microhardness of the alloy decrease when the aging time is increased. The values obtained by applying Treatments C and D are comparable to those obtained by aging for short periods of 2 and 4 h at 240 °C.

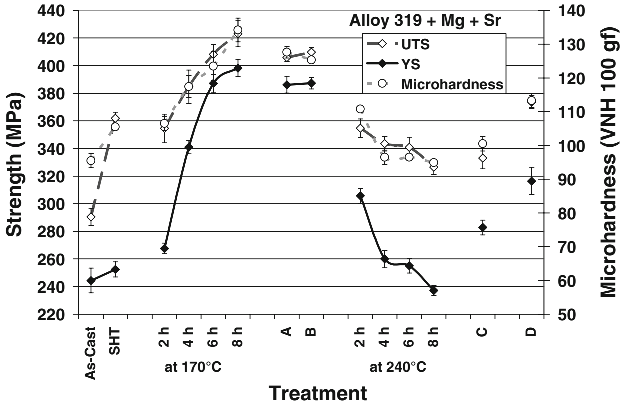

Fig. 1 Ultimate tensile strength *UTS*, yield strength *YS*, and microhardness values for the 319 alloy under various conditions of heat treatment

Precipitation-hardening

The precipitation sequence which occurs during the aging of Al alloys is complex and goes through a number of intermediate stages before the formation of equilibrium precipitates. In Al–Si–Cu–Mg alloys, the precipitation sequences derived from the supersaturated solid solution are generally believed to be as follows: GP zones → θ'' → θ' → θ (Al_2Cu, equilibrium) and GP zones → β'' → β' → β (Mg_2Si, equilibrium) [29, 30]. For a given aging temperature, the sequence and type of phases which form are strongly composition-dependent. Such sequences and types are in turn determined by the equilibrium phases which may eventually form in the alloys.

As-cast condition

Figure 2a shows a micrograph of the microstructure observed in the as-cast material. Since no heat treatment was applied to the alloy, large undissolved particles may be observed in the microstructure. Thus, in the figure, the white arrow indicates the presence of a prominent undissolved Si particle measuring ~0.75 μm. The inset in the image represents the diffraction pattern obtained from the Si particle; the zone axis is $[\bar{1}\,1\,2]$. Figure 2c shows the energy dispersive X-ray spectrum (EDS) of the particle, showing a large Si peak. Figure 2b shows an image obtained from the same sample in scanning transmission electron microscope mode (STEM) where several $TiAl_3$, $Al_{15}(Fe,Mn)_3Si_2$, and undissolved Cu-rich phases are present.

Solution heat-treated condition

Figure 3a–c shows TEM images of the microstructure observed after solution heat treatment. The difference in

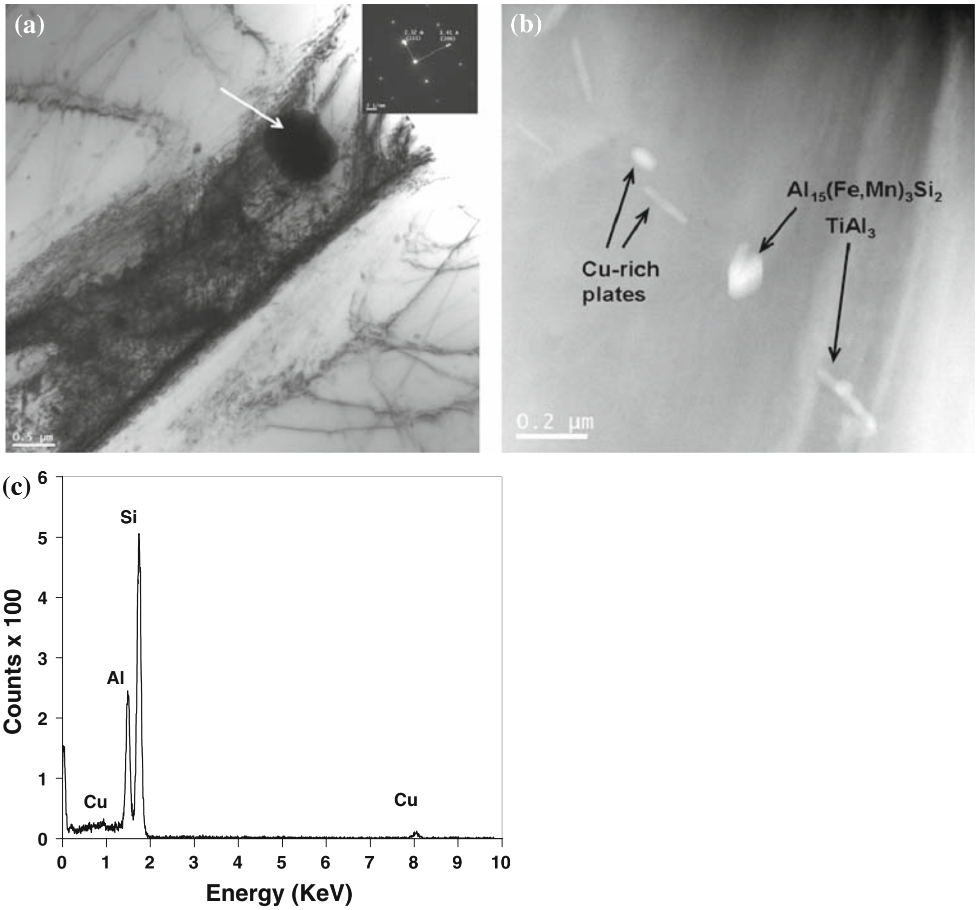

Fig. 2 TEM microstructure observed in the as-cast sample. **a** Bright-field image, the *arrow* points to a Si particle, while the *inset* shows the corresponding diffraction pattern; **b** STEM image showing elongated Cu-rich precipitates, with $TiAl_3$ and $Al_{15}(Fe,Mn)_3Si_2$ particles; **c** EDS spectra of precipitates in **a**

the coefficients of thermal expansion between the matrix and the intermetallic phases observed in the microstructure will cause dislocations to appear. These dislocations release thermal stress generated during quenching from the high solution treatment temperature and tend to form tangles together with the equiaxed Si particles present in the α-Al matrix [9, 30, 31]. Figure 3b shows a dark-field image where precipitates in the form of rods may be observed. Energy dispersive analysis of the precipitates revealed that these are rich in both Cu and Mg indicating that they are possibly the ternary phase S-$CuMgAl_2$ which is not dissolved by the solution treatment [32].

Figure 3c shows a bright-field image of the same sample after solution heat treatment. The image was obtained in the double-beam condition near the [001] zone axis. The morphology of the equiaxed silicon particles may be clearly seen here marked with white arrows. Small β-Mg_2Si plate precipitates which are slightly bigger than the Si equiaxed particles may also be observed. These particles measure approximately 50 × 10 nm which is in accurate mode conformity with the literature [18, 22, 33–37]. These precipitates are marked with black arrows in Fig. 3c. It is possible that the β-phase particles present in the matrix did not dissolve, since the solution temperature required for dissolving the Mg in the alloy is usually higher than the temperature used for this research study [29]. Because alloys of the 319-type contain Cu, the solution temperature should be maintained at a lower level with a maximum of 500 °C to avoid incipient melting of the Cu-rich phases during the solution treatment [38–40], a situation which would be detrimental in terms of the mechanical properties.

Artificial aging condition

The topic of the early mechanisms of the aging process has already been discussed extensively by different researchers [14, 41, 42]. Figure 4 shows a high-magnification bright-field image obtained from the sample aged at 170 °C for 4 h with the electron beam parallel to the [001] zone axis; the inset in the image shows the selected-area diffraction pattern obtained. It will be clearly observed that the GP zones are oriented in the $\langle 001 \rangle$ orthogonal directions of the α-Al matrix. The streaking to be seen along the $\langle 100 \rangle$ directions is a typical indication of the presence of GP zones within the matrix.

Figure 5a shows a low-magnification STEM image of the aged sample in which $TiAl_3$ and Si particles may be observed. The square indicates the area from which the

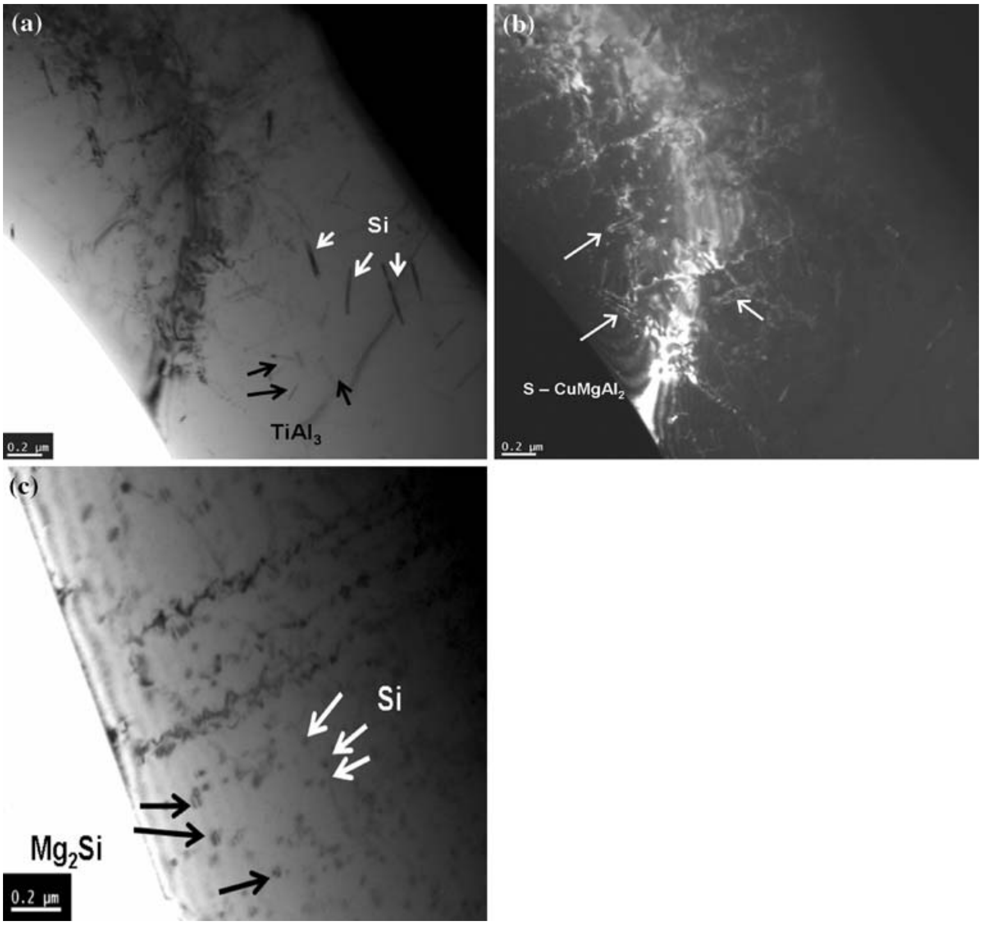

Fig. 3 TEM microstructure of solution heat-treated sample. **a** Bright-field image with low magnification, showing TiAl$_3$; **b** dark-field image, the *arrows* indicate the precipitation of Al$_2$CuMg; **c** bright-field image showing the precipitation of the Mg$_2$Si phase

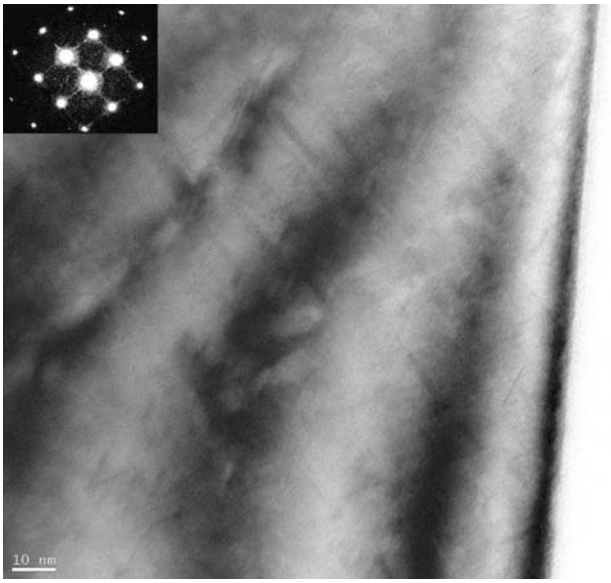

Fig. 4 TEM images of precipitates in the aged sample at 170 °C/4 h, the *inset* is the corresponding selected-area diffraction pattern

X-ray mapping was obtained. It should be noted that the mapping for the Mg Kα energy indicates that this element is distributed throughout the area indicated by the square and that no Mg-containing precipitates may be distinguished. Elements such as Ti, Si, and Cu seem to appear in the same region as the elongated precipitate. Figure 5b, however, shows another STEM image, at high magnification, of a region where the TiAl$_3$, Si, and Cu precipitates appear. From the X-ray mappings, it will be observed that particles containing Si and Cu seem to be located underneath the Ti-containing particle which has a rhomboid shape. The brighter area in the square corresponds to the Cu particle. The Ti present in the alloy comes from the grain refiner used during the casting process, namely, TiB$_2$.

Figure 6a–c shows TEM images, obtained in the double-beam condition near the zone axis [001], showing the microstructure observed in a sample aged at 170 °C for 8 h. This aging condition is the one which yielded the strength and hardness peak. It will be observed that there occurs a dense precipitation of the θ'-Al$_2$Cu metastable

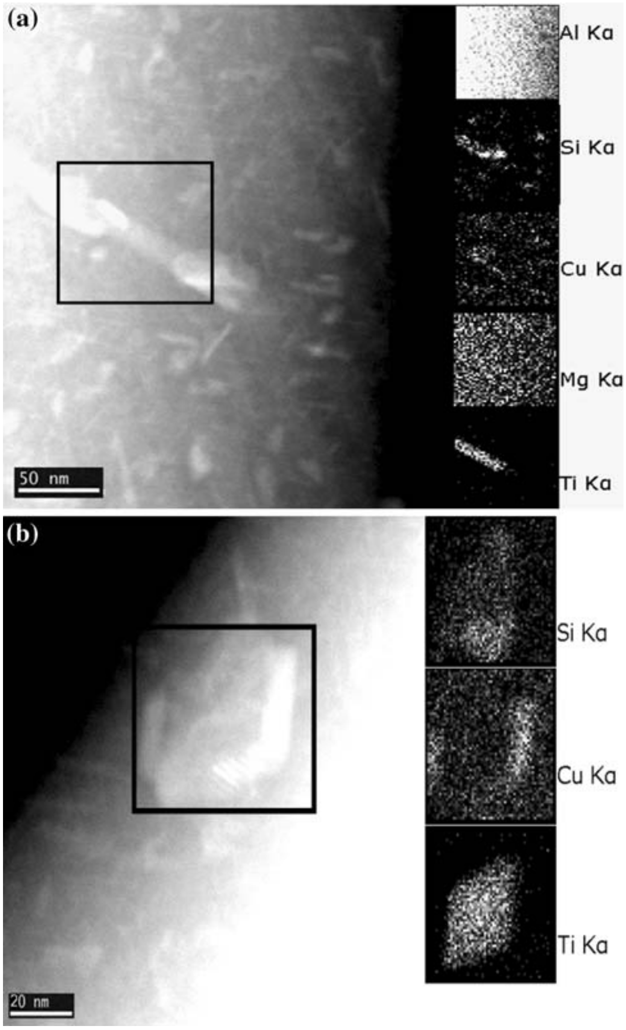

Fig. 5 STEM image of the sample aged at 170 °C/4 h at **a** low magnification and **b** high magnification; the corresponding X-ray mappings of the region are indicated in the *black square*

phase. This behavior is to be expected since Al_2Cu precipitates are the ones responsible for the strengthening mechanism for this type of alloy which was aged to the maximum strength or T6 condition [31, 43]. The plate-like Al_2Cu has an average size of 35 × 5 nm and precipitates in the $\langle 100 \rangle$ directions of the matrix [44].

Figure 7a shows the microstructure which may be observed in a sample treated by means of the overaging condition, that is to say, aged at 240 °C for 8 h. The microstructure consists of plate-like θ-Al_2Cu particles in the α-Al matrix. The image was obtained in the double-beam condition for which the corresponding selected-area diffraction pattern is presented in Fig. 7c, the zone axis being [011]; it should be noted that there are discrete diffraction maxima appearing as additional spots in the diffraction pattern. These additional spots belong to the diffracting planes of the θ-Al_2Cu phase. Figure 7b is a bright-field image showing an area of Fig. 7a at high magnification, where the θ-Al_2Cu particles may easily be examined. These particles precipitate in the orthogonal $\langle 100 \rangle$ directions of the matrix. Electron diffraction spectra and X-ray maps were obtained to elucidate compositional information from the precipitates observed in the figure.

Figure 8a presents an STEM image of the microstructure observed in samples having undergone an overaging treatment accompanied by the corresponding X-ray maps for the different elements present in the alloy. The X-ray maps relate to the area indicated by the white square in the STEM image. As expected, the aluminum map indicates that this element is present throughout the area; silicon particles in the form of equiaxed precipitates may also be seen, indicated by black arrows in the image. These equiaxed Si particles do not grow any larger than 50 nm even after the application of overaging treatments such as aging at 240 °C for 8 h. The white arrows indicate where the Cu plates may be observed. The Mg map indicates the Mg-content of the tiny plates measuring ~20 × 5 nm observed close to the Cu-containing plates. The map for Ti indicates that it is not present in this area; thus, large $TiAl_3$ rods were not observed in the instance of this particular aging condition.

Figure 8b shows a further STEM image at high magnification where an X-ray line scan was taken along the black line AB, from points A to B. Figure 8c shows a graph depicting the intensity of the characteristic X-rays emitted by Al, Si, Cu, and Mg along the line scan path AB shown in Fig. 8b. It will be observed that the plate-like particle contains Al and Cu; the next particle could potentially be a small needle of the quaternary phase Q-($Al_5Cu_2Mg_7Si_7$) since the intensity of all the elements presented in the graph increases; this type of particle, however, would be present only as a minor species [18, 45]. It has been reported, for other cast alloys such as alloy 339, that particles of the quaternary phase Q tend to nucleate on Si particles [18]. The average size of the Q phase is 50 × 5 nm.

Comparison between conventional and non-conventional aging cycles

Figure 9a and b illustrates the comparison between a sample which was aged continuously to obtain a peak-aged condition by applying a T6 treatment at 170 °C for 8 h, and a sample which had been aged by applying a T6-type multi-temperature aging cycle of 2 h at 190 °C followed by 5 h at 180 °C, respectively. The values obtained for UTS, YS, and microhardness were slightly lower for the sample aged by means of the multi-temperature treatment; thus, 406 MPa UTS, 386 MPa YS, and 128 VHN compared to 423 MPa UTS, 398 MPa YS, and 134 VHN in the case of the former treatment. A comparison of Fig. 9a and b will

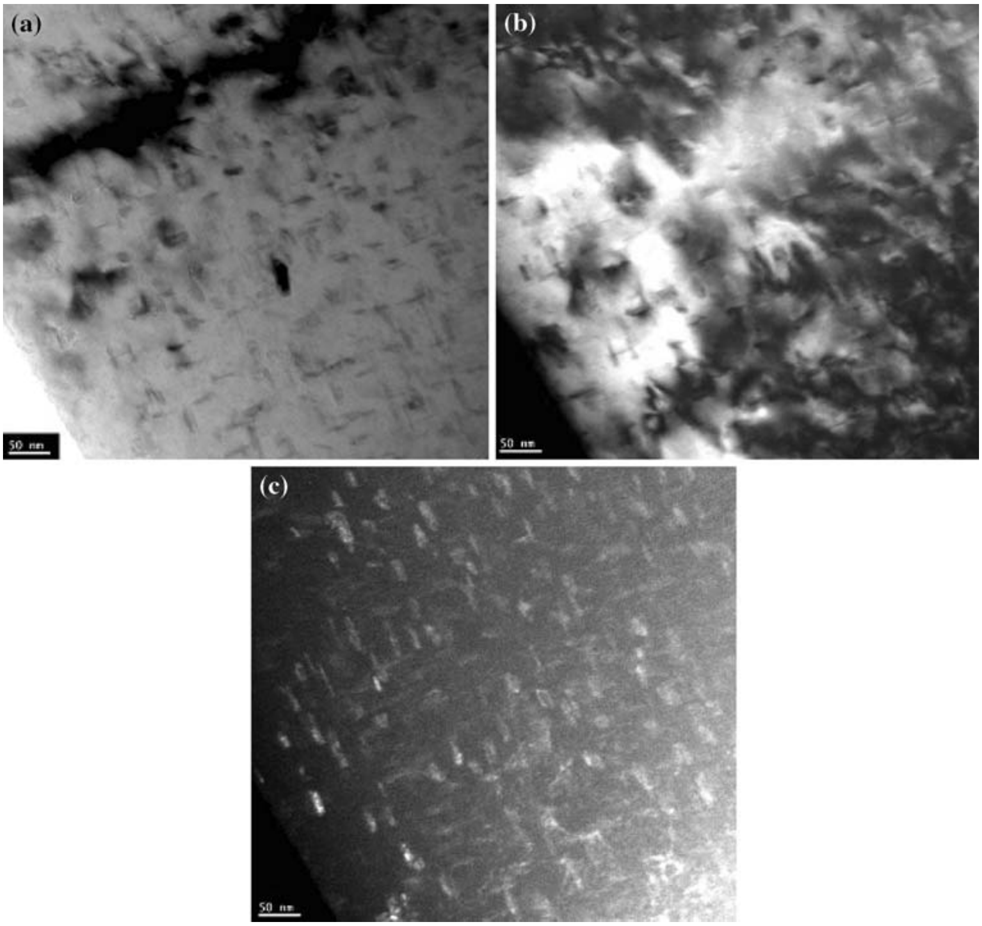

Fig. 6 TEM microstructures of aged sample at 170 °C/8 h. **a** Bright-field image, **b** dark-field image, **c** STEM

reveal that the plate-like particles are more widely spaced in the sample previously aged with a multi-temperature treatment, as shown in Fig. 9b, than they are in the sample aged using the continuous T6 aging treatment, shown in Fig. 9a.

Figure 10a and b shows the comparison between a sample which was aged using Treatment A, namely, 2 h at 190 °C and 5 h at 180 °C, and a sample which was aged using the same treatment but with the addition of an intermediate interruption stage at room temperature, that is to say, 2 h at 190 °C, 100 h at 25 °C, and 5 h at 180 °C. Figure 10c and d shows the comparison between a sample aged by the application of a continuous T7 treatment, 2 h at 240 °C, in contrast with a sample which had been submitted to aging through a T7-type multi-temperature treatment, in other words, for 1 h at 170 °C, 1 h at 190 °C, and then 2 h at 240 °C. It will be observed from Fig. 10c that when overaging is instigated, a characteristic coarsening of the Al_2Cu plates occurs. This coarsening will lead to the same type of microstructure as was presented in Fig. 7b which shows a higher density of coarse Cu-containing precipitates; this figure corresponds to the thoroughly overaged material which had been aged at 240 °C for 8 h. Both the bright-field images presented in Fig. 10c and d were obtained using the double-beam condition with the transmitted beam parallel to the [001] zone axis. The equiaxed precipitates observed in both the images correspond to the S-$CuMgAl_2$ ternary phase. More of these precipitates may be observed in Fig. 10d. These particles display a rod-like morphology, where the rods measure about 100 nm in length and 10 nm in thickness. The orientation of this phase is parallel to the zone axis of the images and will, therefore, appear as dots or equiaxed particles [18, 32, 46, 47].

It will also be observed that the coarsening of the Al_2Cu plates is not present in Fig. 10d and that there is still a high concentration of plate-like precipitates. This behavior indicates that the inclusion of certain underaging stages before the actual overaging stage would be beneficial to the material since it delays the overaging process. Such a delay could be explained by the fact that underaging carried out at lower temperatures ranging from 150 to 190 °C would cause nucleation of the early metastable phases. Later on, when the temperature has risen to the overaging

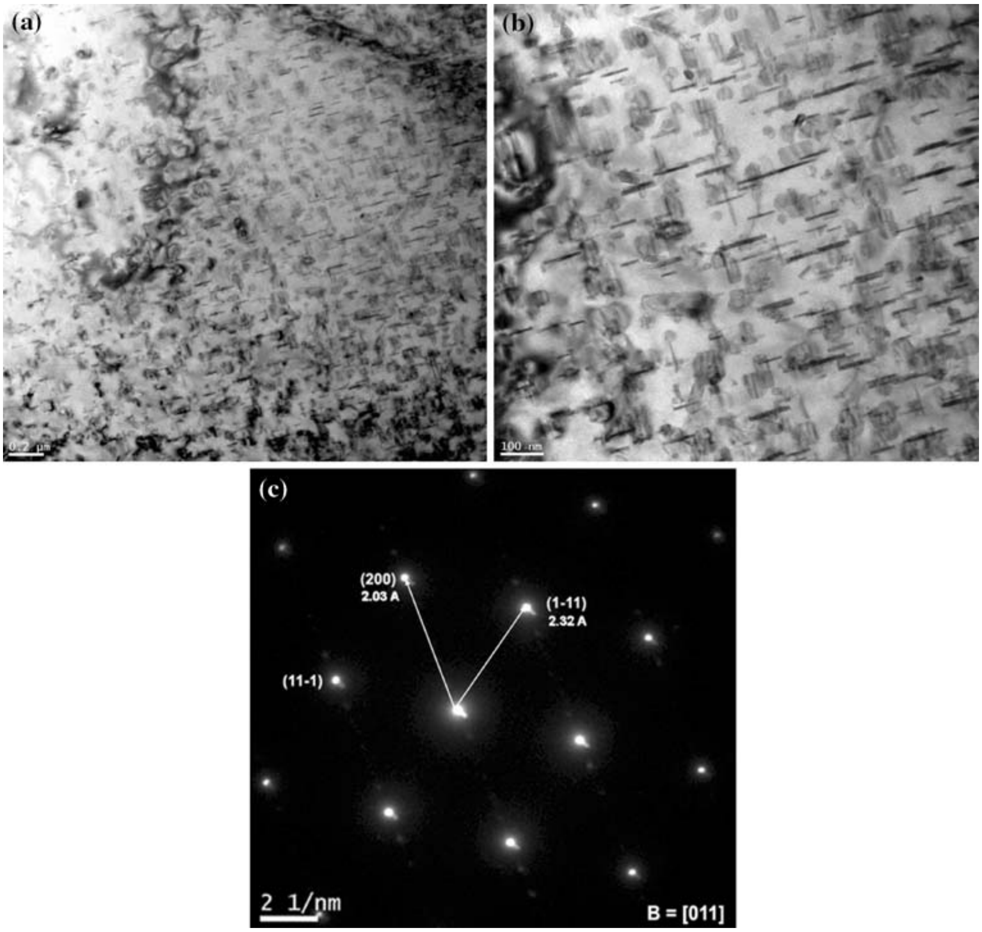

Fig. 7 TEM microstructures of aged sample at 240 °C/8 h (overaging). **a** Bright-field image at low magnification, **b** bright-field image at high magnification, **c** selected-area diffraction pattern of θ-Al_2Cu phase

temperature, or 240 °C, these metastable phases will disappear. Subsequently there will be a local enrichment of the atoms contained in the metastable phases, however, which in turn will produce a smaller and better distributed stable phase during overaging, thereby improving the mechanical properties of the material to some extent.

The application of an underaging stage before overaging does not always improve the mechanical properties. Figure 10e shows a bright-field TEM image obtained from a sample aged by means of Treatment C, namely, 24 h at 130 °C and 2 h at 240 °C. This multi-temperature treatment yielded lower property values than did the continuous T7 overaging cycle (333 MPa UTS, 283 MPa YS, and 100 VHN compared with 355 MPa UTS, 306 MPa YS, and 110 VHN). The image was obtained using the double-beam condition, with the transmitted beam parallel to the [001] zone axis. The microstructure observed in the sample shows Al_2Cu plates still presenting a homogeneous distribution in the matrix. Some Al_2Cu plates may also be observed in the form of thick plates, indicating that the transformation of the metastable θ'-Al_2Cu to the stable θ_{eq} has occurred. The Al_2Cu plates are indicated in Fig. 10e by the white arrows. The darker particles present in the microstructure consist of Si plates; these are indicated by the black arrows. Rod-like S-$CuMgAl_2$ precipitates are also present in the structure, as marked by the dotted black arrows. The coarsening of strengthening precipitates such as Al_2Cu, Mg_2Si, $CuMgAl_2$, and so forth, may have a detrimental effect on the mechanical properties of the alloy. This behavior is to be expected, since the underaging stage of the multi-temperature treatment is relatively long, namely, 24 h; there is, however, sufficient time for these phase precipitates to coarsen and form the thick plates and particles which may be observed in Fig. 10e.

Conclusions

The following conclusions may be drawn from observation of the microstructures as made in this study on the precipitation-hardening behavior of 319 alloys:

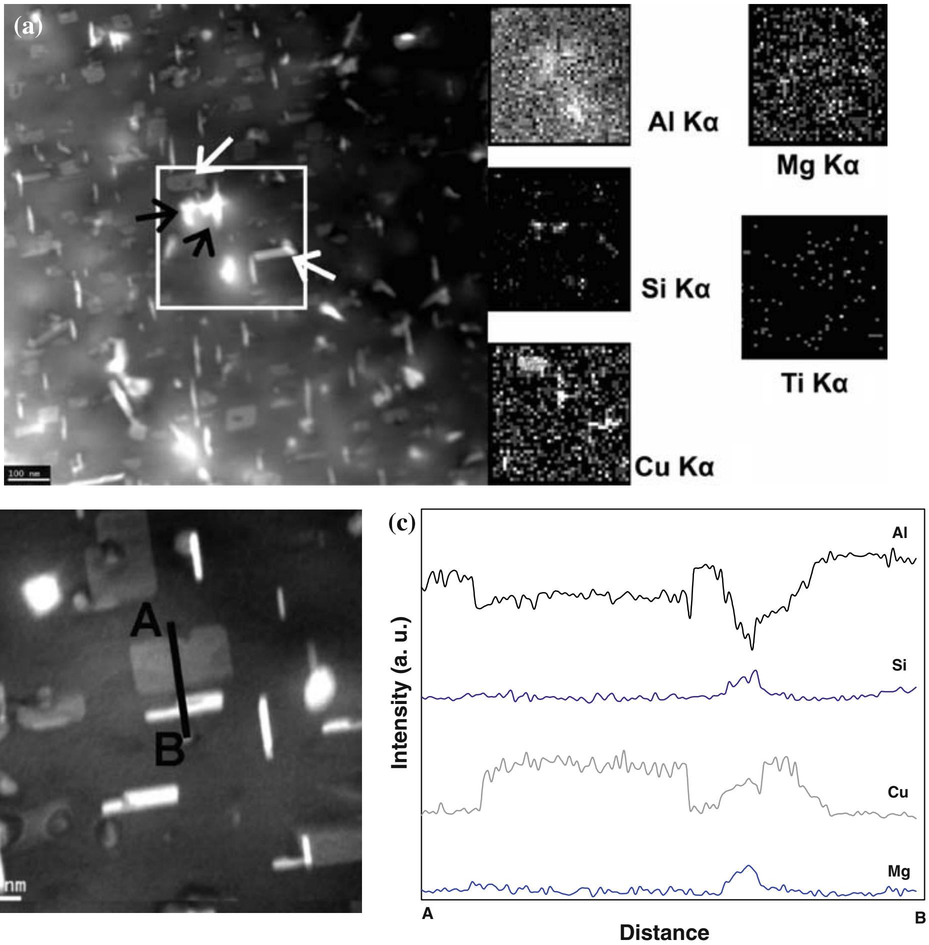

Fig. 8 STEM image of the aged sample at 240 °C/8 h at **a** low magnification, the corresponding X-ray mappings of the region are indicated in the *black square*; **b** high magnification, showing the area from which X-ray maps and a line scan were obtained; **c** graph of the X-ray intensities obtained across the line scan *AB* indicated in **b**

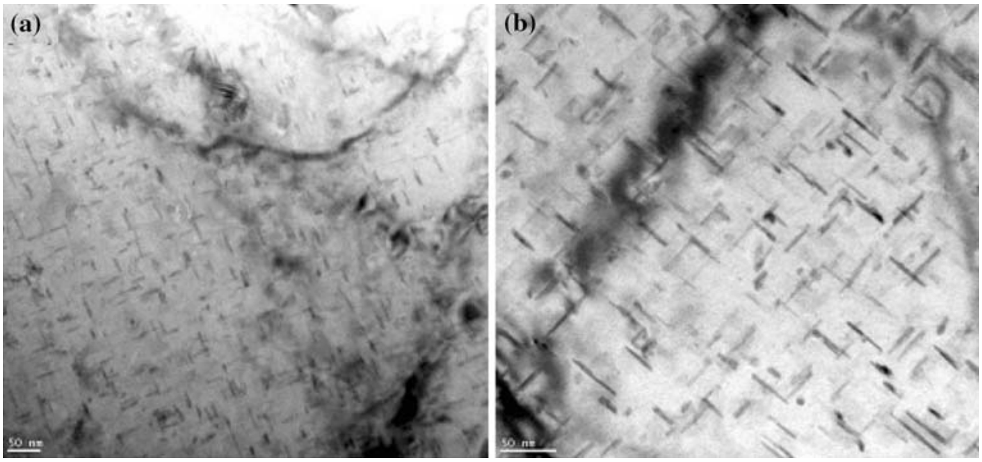

Fig. 9 Bright-field TEM images of **a** peak-aged sample (170 °C/8 h), **b** sample aged at 190 °C/2 h + 180 °C/5 h

1. Precipitates of $CuMgAl_2$ and Mg_2Si were identified in the solution heat-treated alloy; these phases, however, are present only as a minor species. Another feature observed was the presence of dislocation tangles which appear as a result of the difference in coefficients of thermal expansion between the matrix and the intermetallic phases present. Dislocations release thermal stress generated during quenching from high solution treatment temperatures, and they tend to form tangles together with the equiaxed Si particles present in the α-Al matrix.
2. The peak aging condition, or aging at 170 °C for 8 h, shows a dense homogeneous precipitation of θ'-Al_2Cu plates which are the main contributor to strengthening

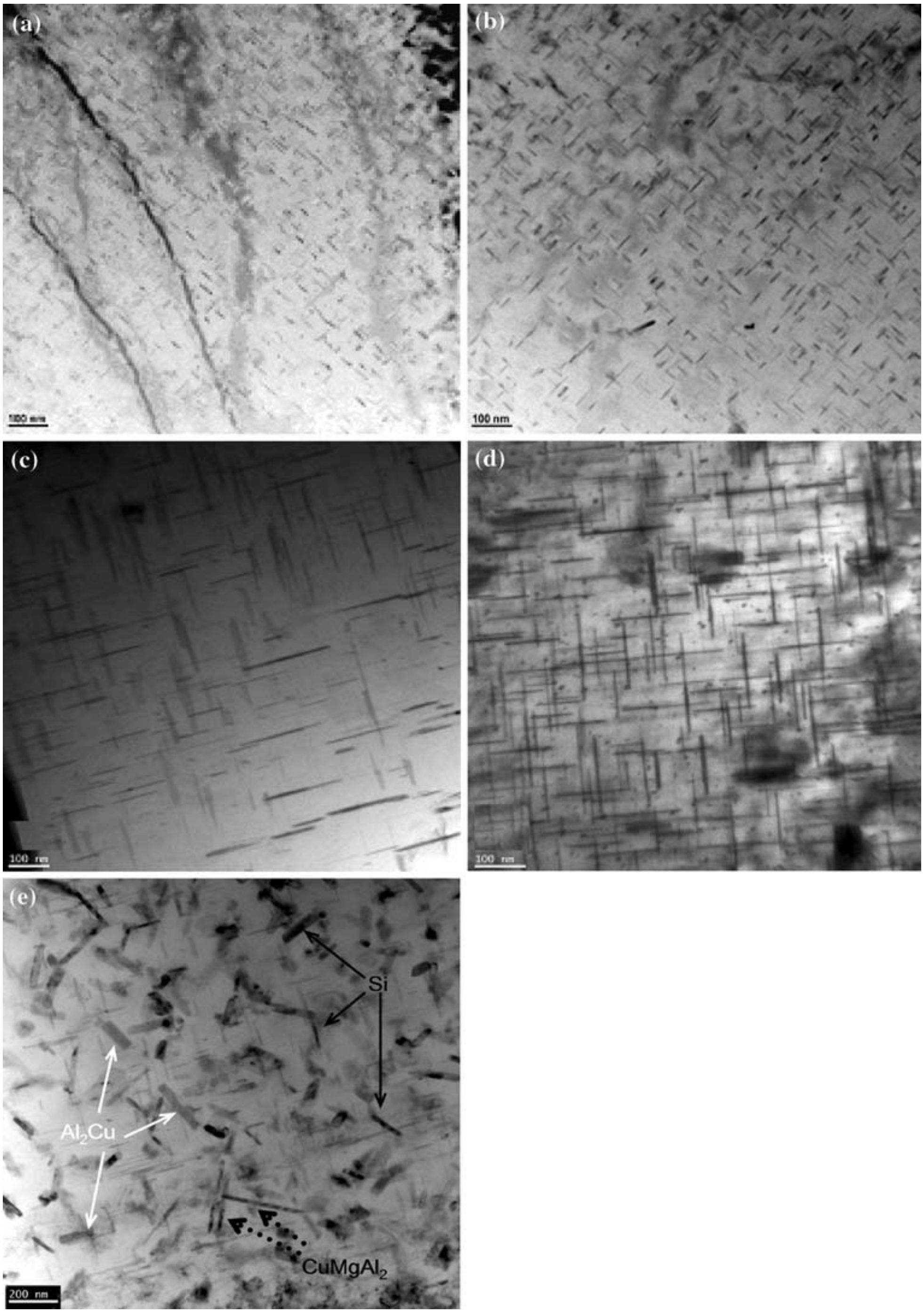

Fig. 10 TEM images of precipitates in the samples at different aging stages. **a** 190 °C/2 h + 180 °C/5 h, **b** 190 °C/2 h + 25 °C/100 h + 180 °C/5 h, **c** 240 °C/2 h, **d** 170 °C/1 h + 190 °C/1 h + 240 °C/2 h, **e** 130 °C/24 + 240 °C/2 h

in 319-type alloys, oriented in the ⟨100⟩ directions of the matrix; these plates display an average size of 35 × 5 nm.

3. The wide spacing between the Al_2Cu precipitates observed in the sample aged by means of a T6-type non-conventional treatment explains why this treatment does not further improve the properties obtained by conventional T6 treatment (aging at 170 °C for 8 h). A dense precipitation of intermetallic species will impede the movement of dislocations through the matrix, thereby increasing the strength of the material; when the precipitates are widely dispersed the dislocations can cross between them easily.

4. Including an interruption stage in multi-temperature aging cycles does not have any effect on 319-type alloys, as evidenced by the corresponding mechanical properties and observation of the microstructure.
5. The properties obtained using the conventional T7 treatment (240 °C for 2 h) may be improved upon slightly (cf. Fig. 1) by applying non-conventional aging cycles such as Treatment D: 1 h at 170 °C + 1 h at 190 °C + 2 h at 240 °C. The corresponding microstructure for the sample treated with Treatment D shows a high concentration of plate-like Al_2Cu precipitates, indicating that the inclusion of certain underaging stages before the overaging stage can delay the overaging process.
6. The application of Treatment C, 24 h at 130 °C + 2 h at 240 °C, does not yield improved properties as compared to the conventional T7 treatment. The corresponding microstructure shows that coarse Al_2Cu, Si, and $CuMgAl_2$ plates are present in the α-Al matrix and are detrimental to the mechanical properties of the alloy.

Acknowledgements The authors would like to express their gratitude to the Natural Sciences and Engineering Research Council of Canada (NSERC), to General Motors Powertrain Group (USA), and to Corporativo Nemak (Mexico) for the financial support and in-kind help provided for carrying out this research. Help provided by Dr. Agnes M. Samuel in correcting the manuscript is greatly appreciated.

References

1. Kaufman JG (2000) Introduction to aluminum alloys and tempers. ASM International, Materials Park, p 108
2. Chang J, Moon I, Choi C (1998) J Mater Sci 33:5015. doi:10.1023/A:1004463125340
3. Komiyama Y, Uchida K, Gunshi M (1976) J Jpn Inst Light Met 26:311
4. Basavakumar KG, Mukuda PG, Chakraborty M (2007) J Mater Sci 42:8714. doi:10.1007/s10853-007-1754-z
5. Yu L, Liu X, Wang Z, Bian X (2005) J Mater Sci 40:3865. doi:10.1007/s10853-005-2893-8
6. Gruzleski JE, Closset B (1990) The treatment of liquid aluminum silicon alloys. American Foundrymen's Society, Des Plaines, p 31
7. Samuel FH, Samuel AM, Liu L (1995) J Mater Sci 30:2531. doi:10.1007/BF00362130
8. Tavitas-Medrano FJ, Gruzleski JE, Samuel FH, Valtierra S, Doty HW (2008) Mater Sci Eng A 480:356
9. Kang HG, Kida M, Miyahara H, Ogi K (1999) AFS Trans 107:507
10. Weakley SC, Donlon W, Wolverton C, Jones JW, Allison JE (2004) Metall Mater Trans A 35A:2407
11. Cáceres CH (2000) J Mater Eng Perform 9:215
12. Ouellet P, Samuel FH (1999) J Mater Sci 34:4671. doi:10.1023/A:1004645928886
13. Hatch JE (1984) Aluminum: properties and physical metallurgy. American Society for Metals, Materials Park, p 143
14. Abis S, Massazza M, Mengucci P, Riontino G (2001) Scripta Mater 45:685
15. Mishra RK, Smith GW, Baxter WJ, Sachdev AK, Franetovic V (2001) J Mater Sci 36:461. doi:10.1023/A:1004888831537
16. Barlow IC, Rainforth WM, Jones H (2000) J Mater Sci 35:1413. doi:10.1023/A:1004767131956
17. Wang G, Sun Q, Feng L, Hui L, Jing C (2007) Mater Des 28:1001–1005
18. Mishra RK, Sachdev AK, Baxter WJ (2004) AFS Trans 112:179
19. Chakrabarti DJ, Laughlin DE (2004) Prog Mater Sci 49:389
20. Eskin DG (2003) J Mater Sci 38:279. doi:10.1023/A:1021109514892
21. Shivkumar S, Ricci S, Apelian D (1990) AFS Trans 98:913
22. Hernandez-Paz JF, Paray F, Gruzleski JE, Emadi D (2004) AFS Trans 112:155
23. Zhang DL, Zheng L (1996) Metall Mater Trans A 27A:3983
24. Wang QG, Davidson CJ (2001) J Mater Sci 36:739. doi:10.1023/A:1004801327556
25. Lumley RN, Morton AJ, O'Donnell G, Polmear IJ (2004) Ind Heat 71:31
26. Lumley RN, Polmear IJ, Morton AJ (2002) Mater Sci Forum 396–402:893
27. Lumley RN, Polmear IJ, Morton AJ (2003) Mater Sci Technol 19:1483
28. Lumley RN, Polmear IJ, Morton AJ (2005) Mater Sci Technol 21:1025
29. Kaufman JG, Rooy EL (2004) Aluminum alloy castings: properties, processes, and application. ASM International, Materials Park, p 13
30. Martin JW (1998) Precipitation hardening, 2nd edn. Butterworth-Heinemann, Oxford, p 79
31. Gladman T (1999) Mater Sci Technol 15:30
32. Ratchev P, Verlinden B, Van Houtte P (1994) Scripta Metall Mater 30:599
33. Kido K, Matsuda K, Kawabata T, Sato T, Ikeno S (2002) Mater Sci Forum 396–402:953
34. Murayama M, Hono K (1999) Acta Mater 47:1537
35. Gupta AK, Lloyd DJ, Court SA (2001) Mater Sci Eng A316:11
36. Esmaeili S, Wang X, Lloyd DJ, Poole WJ (2003) Metall Mater Trans 34A:751
37. Murayama M, Hono K, Saga M, Kikuchi M (1998) Mater Sci Eng A250:127
38. Samuel FH (1998) J Mater Sci 33:2283. doi:10.1023/A:1004383203476
39. Wang G, Bian X, Wang W, Zhang J (2003) Mater Lett 57:4083
40. Li Z, Samuel AM, Samuel FH, Ravindran C, Valtierra S, Doty H (2003) AFS Trans 111:241
41. Ringer SP, Hono K, Polmear IJ, Sakurai T (1996) Appl Surf Sci 94:253
42. Ringer SP, Hono K, Sakurai T, Polmear IJ (1997) Scripta Mater 36:517
43. Polmear IJ (2001) Mater Sci Forum 363–365:1
44. Porter DA, Easterling KE (1981) Phase transformations in metals and alloys, 1st edn. Van Nostrand Reinhold (UK) Co. Ltd, Wokingham, p 263
45. Cayron C, Buffat PA (2000) Acta Mater 48:2639
46. Miao WF, Laughlin DE (2000) Metall Mater Trans 31A:361
47. Ratchev P, Verlinden B, DeSmet P, Van Houtte P (1999) Mater Trans JIM 40:34